RESEARCH ARTICLE

Check for updates

Synthesis of broadband NIR garnet phosphor Ca₄ZrGe₃O₁₂: Cr³⁺, Yb³⁺ for NIR pc-LED applications

Jinmeng Xiang,[a] Jiming Zheng, [iD][a] Xiaoqi Zhao,[b] Xue Zhou,[a] Changheng Chen,[a] Minkun Jin[a] and Chongfeng Guo [iD] *[a]

There are outstanding application prospects for near-infrared phosphor-converted light-emitting diodes (NIR pc-LEDs) in many fields such as non-destructive detection, bio-imaging, and modern agriculture, in which the development of NIR-emitting phosphors with large full width at half maximum (FWHM), high efficiency, and excellent thermal stability is the challenge of current research. Herein, a broadband NIR-emitting phosphor Ca₄ZrGe₃O₁₂: Cr³⁺ (CZGO: Cr³⁺) was successfully synthesized, which ranged from 650 to 1250 nm with 160 nm FWHM under the excitation of blue light at 477 nm. Based on the first-principles theory calculation, the origination of its matrix luminescence was accurately predicted, and the site-selective occupancy and the formation of various charge transfer bands (CTBs) have also been revealed in detail. With the introduction of Yb³⁺ into CGZO: Cr³⁺, the FWHM was broadened to 230 nm, and the thermal stability was also significantly increased. Furthermore, a NIR pc-LED device was fabricated by combining CZGO: Cr³⁺/Yb³⁺ with a 450 nm commercial LED chip, and it demonstrated satisfactory performance in night vision and bio-imaging.

1. Introduction

There is currently great interest in broadband near-infrared (NIR) light sources due to their numerous applications in bio-imaging, non-destructive detection, and night vision.[1–5] Low efficiency and large size are always associated with traditional NIR light sources such as halogen lamps and tungsten filaments, while AlGaAs light-emitting diodes (LEDs) can achieve a NIR light with excellent efficiency and small size.[6,7] However, bio-imaging and composition detection require a broadband NIR light source to expand the testing scope and obtain additional information,[8–10] but the narrow full width at half maximum (FWHM) of AlGaAs LEDs (FWHM < 50 nm) limits their use in various practical applications. Thus, there has been increased interest in the newly emerged NIR phosphor-converted light-emitting diodes (pc-LEDs).[11] By combining a commercial blue LED chip with a NIR-emitting phosphor, the fabricated LED device can realize a broadband NIR light with the advantages of high efficiency, low cost, and small size. However, there is a very large Stokes shift of the luminous

center because of the huge energy difference between the emission and excitation light, which will inevitably produce a strong thermal effect, chromatic drift, and reduction in luminous intensity.[12] Therefore, a thermally stable broadband NIR phosphor has become the main challenge at this stage.

Currently, a large number of Cr³⁺-doped NIR phosphors have been reported that can easily achieve a broadband NIR emission in a weak crystal field environment, such as Ca₂LuScGa₂Ge₂O₁₂: Cr³⁺ (FWHM = 150 nm) and LiInSi₂O₆: Cr³⁺ (FWHM = 143 nm).[13,14] Multi-site occupancy of Cr³⁺ can also realize a broadband NIR emission, but the weak crystal field environment is still essential. Xie's group created La₂MgZrO₆: Cr³⁺ (FWHM = 210 nm), in which Cr³⁺ simultaneously occupied the Mg/ZrO₆ octahedron sites and consequently emitted a broadband NIR light.[15] Additionally, Yb³⁺ is always used to broaden the FWHM by the efficient energy transfer from Cr³⁺ to Yb³⁺, and thermal stability can also be increased because of its simple energy levels, which effectively avoid the energy loss from cross-relaxation between different energy levels.[16–19]

As Zhang's group reported, the FWHM of the garnet-structured phosphor Ca₂LuZr₂Al₃O₁₂: Cr³⁺ can be broadened from approximately 160 to 340 nm by the efficient energy transfer from Cr³⁺ to Yb³⁺, and the thermal stability ($T_{0.5}$) can also be greatly increased from 450 to 650 K by introducing a high concentration of Yb³⁺.[20] Notably, the garnet structure is always considered as an excellent and stable thermal matrix,

[a] State Key Laboratory of Photon Technology in Western China Energy, Institute of Photonics & Photon Technology, Northwest University, Xi'an, 710069, China. E-mail: guocf@nwu.edu.cn

[b] School of Physics and Opto-Electronic Technology, Baoji University of Arts and Sciences, Baoji, Shaanxi, 721016, China

and it is expected to be an ideal host for overcoming severe thermal quenching resulting from the huge Stokes shift of Cr^{3+}, such as in $Na_3In_2Li_3F_{12}$: Cr^{3+} (82%@423 K)[21] and $Gd_3Sc_2Ga_3O_{12}$: Cr^{3+} (92%@423 K).[22] Therefore, Cr^{3+} and Yb^{3+} co-doped garnet-structured hosts are ideal for exploring broadband NIR-emitting phosphors with satisfactory thermal stability.

In this work, a garnet-structured phosphor CZGO: Cr^{3+}, Yb^{3+} was prepared, in which the site selection occupancy of Cr^{3+} and Yb^{3+} was confirmed by the first-principles theory calculation. According to the partial density of states (PDOS) of the CZGO host, the host luminescence was identified as the electron transition generated by orbital coupling between the Zr and O atoms. Under the excitation of blue light at 477 nm, CZGO: Cr^{3+} showed a broadband (FWHM = 160 nm) NIR emission from 650 to 1250 nm, centered at 840 nm. Utilizing the introduction of Yb^{3+}, the FWHM was broadened to 230 nm, and then, the thermal stability significantly increased. The energy transfer process between Cr^{3+} and Yb^{3+} was subsequently investigated by spectroscopy and decay curves. Combined with a commercial 450 nm LED chip, the fabricated LED device output a bright NIR light that provided a satisfactory performance when used for night vision and bio-penetration. These results illustrate that CZGO: Cr^{3+}, Yb^{3+} possesses the potential for application in night vision and bio-imaging.

2. Experimental

2.1 Synthesis of samples

Phosphors CZGO: x% Cr^{3+}, y% Yb^{3+} (x = 0, 0.6, 0.8, 1.0, 1.2, 1.5, 2.0; y = 0, 1, 2, 3, 4) were synthesized via a high-temperature solid-state reaction method. The stoichiometric analytical reagent (A. R.) raw materials $CaCO_3$, ZrO_2, Cr_2O_3, and high purity (99.99%) GeO_2 and Yb_2O_3 were first ground for 20 min with a small amount of ethanol. Next, the mixture powder was pre-sintered at 650 °C for 2 h and sintered at 1400 °C for 4 h in air. Finally, the samples were obtained after natural cooling to room temperature.

2.2 Characterization

Powder X-ray diffraction (XRD) data was collected on Bruker D8 Advance powder diffractometer (Bruker Corporation, Germany) at 40 kV and 30 mA with Cu Kα radiation (λ = 1.5405 Å), and the step size of 2θ was 0.02°. Rietveld refinement was performed by General Structure Analysis System (GSAS) software.[23] The diffusion reflection spectra (DRS) were measured by a ultraviolet-visible (UV-Vis) spectrophotometer (Cary 5000). The photoluminescence (PL) and excitation (PLE) spectra as well as the decay curves were obtained using an Edinburgh FLS920 fluorescence spectrophotometer (Edinburgh Instruments Ltd, UK) equipped with 450 W Xe lamp and a microsecond flash-lamp (uF920H) as a light source, respectively. The quantum yield (QY) was tested by the integrating sphere on the same Edinburgh FLS920 fluorescence spectrophotometer with $BaSO_4$ as a reference. The temperature-dependent PL spectra (280–470 K) and a low-temperature spectrum at 4 K were

obtained with an Oxford OptistatDN2 nitrogen cryogenics temperature controller and the Oxford OptistatDry system, respectively.

2.3 Computational details

The computation was performed by CASTEP.[24] The band structure, partial density of states (PDOS), and formation energy were calculated by density functional theory (DFT) in the form of the generalized gradient approximation (GGA) Perdew–Burke–Ernzerhof (PBE) function.[25] A Monkhorst–Pack $3 \times 3 \times 2$ κ mesh was used as the Brillouin zone, and the kinetic energy cutoff and SCF were set as 500 eV and 10^{-5} eV per atom, respectively.

3. Results and discussion

3.1 Phase and structure

To verify the phase purity, powder XRD Rietveld refinements of blank and Cr^{3+}/Yb^{3+} co-doped CZGO were representatively performed. Fig. 1a and b show that all Bragg reflections coincided well with those of the calculated data, and residual factors were low (R_{wp} = 8.3% and R_p = 6.1% for the blank sample; R_{wp} = 9.0% and R_p = 6.5% for Cr^{3+}/Yb^{3+} co-doped CZGO). Accordingly, the samples were successfully synthesized, and Cr^{3+}/Yb^{3+} entered into the host. The crystallographic parameters are listed in Table 1. As depicted in Fig. 1c, the garnet structure CZGO exhibits characteristics of a cubic phase with the $Ia\bar{3}d$ space group. There are four Wyckoff sites, 24c, 16a, 24d, and 96h, which are occupied by Ca1, Ca2/Zr, Ge, and O, respectively. In particularly, Ca1 is coordinated with 8 oxygen atoms, and Ca2 and Zr equally share the 16a site with a coordination number (CN) of 6. Theoretically, Cr^{3+}/Yb^{3+} [CN = 6, $r(Cr^{3+})$ = 0.615 Å, $r(Yb^{3+})$ = 0.868 Å; CN = 8, $r(Yb^{3+})$ = 0.985 Å] can occupy the $Ca1O_8$ [CN = 8, $r(Ca^{2+})$ = 1.12 Å] and Ca_2/ZrO_6 [CN = 6, $r(Ca^{2+})$ = 1.00, $r(Zr^{4+})$ = 0.720 Å] sites due to their close radius and valence.[26] To confirm the site occupancy selection of Cr^{3+} and Yb^{3+}, the formation energy (E_{form}) was computed by the first-principles theory calculation according to the following equation:

$$E_{form} = E_{doped} - E_{pure} - n \times E_{dopant} + m \times E_{atom}$$

$$(1)$$

where E_{doped} and E_{pure} represent the total energy of the host with or without dopant, respectively; E_{dopant} and E_{atom} denote the atomic energy of the dopant and the atom replaced by dopant, respectively; n and m denote the number of the dopant and the atom replaced by dopant, respectively. Obviously, the Cr substituting for Zr possesses the lowest E_{form} (−9.5 eV), implying that it is most likely that Cr^{3+} will occupy the ZrO_6 site.[27] Likewise, the Yb^{3+} prefers to enter into the $Ca1O_8$ (E_{form} = −6.5 eV) site than others (Fig. 1d).

The diffusion reflection spectra (DRS) of the blank, and CZGO singly or co-doped with Cr^{3+}/Yb^{3+} are illustrated in Fig. 2a. Except for the matrix absorption band at approximately 220 nm, a Zr–O charge transfer band (CTB) is observed at 280 nm in the CZGO host. The DRS of Yb-doped CZGO is similar to that of the blank host, but a slight absorption
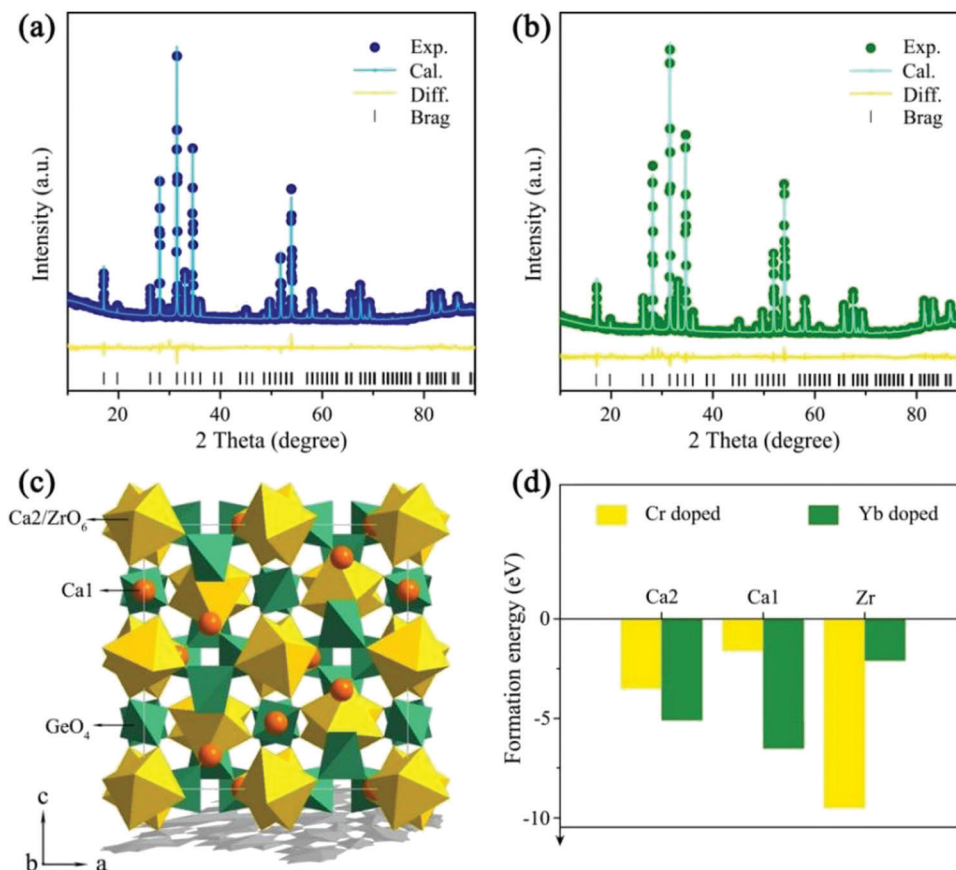
Fig. 1 Powder XRD Rietveld refinements of (a) blank CZGO and (b) CZGO: 1% Cr^{3+}, 1% Yb^{3+}; (c) the crystalline structure and cationic sites in CZGO; (d) the formation energy of Cr or Yb doped into the different cationic sites $Ca1O_8$, $Ca2/ZrO_6$, and GeO_4.

Table 1 Rietveld refinement and crystallographic parameters of the CZGO blank and CZGO: 1% Cr^{3+} and 1% Yb^{3+}

Compound	CZGO	CZGO: 1% Cr^{3+} and 1% Yb^{3+}
Space group	$Ia\bar{3}d$	$Ia\bar{3}d$
a/c, Å	12.7	12.7
V, Å^3	2057.5	2055.3
R_{wp}, %	8.3	9.0
R_p, %	6.1	6.5
χ^2	2.1	2.3

enhancement at 280 nm is likely caused by Yb–O CTB. On the contrary, a significant absorption band occurs at 260 nm in the Cr^{3+}-doped sample that belongs to Cr–O CTB. Other absorption bands at 390, 477, and 680 nm correspond to transition $^4A_2(G)$–$^4T_1(P)$, $^4A_2(G)$–$^4T_1(F)$, and $^4A_2(G)$–$^4T_2(F)$ of Cr^{3+}, respectively. The Cr^{3+} singly doped and Cr^{3+}/Yb^{3+} co-doped samples exhibit similar DRS, meaning that there is efficient energy transfer from the Cr^{3+} to Yb^{3+} ions. The optical band gap can be estimated by the Kubelka–Munk function:[28]

$$F(R) = \frac{(1-R)^2}{2R} \tag{2}$$

$$(\alpha h\nu)^n = A(h\nu - E_g) \tag{3}$$

$$[h\nu F(R_\infty)]^2 = A(h\nu - E_g) \tag{4}$$

where R denotes the diffuse reflectance, $h\nu$ denotes the photon energy, and A represents an absorption constant. For the direct and indirect band gap, n is equal to 2 and 1/2, respectively. Based on the following first-principles theory calculation, CZGO is characterized by a direct band gap. The band gap was calculated to be 5.2, 5.1, 4.9, and 4.8 eV for the blank, Yb^{3+}-doped, Cr^{3+}-doped, and Cr^{3+}/Yb^{3+} co-doped sample, respectively (Fig. 2b).

To further confirm the contribution of CTBs in Fig. 2a and reveal the composition of the conduction (CB) and valence band (VB), the band structure and PDOS were calculated by the first-principles theory calculation. As shown in Fig. 3a, the CZGO is characterized by a direct band gap, and the band gap (E_g) is 3.50 eV, which is smaller than that of the experimental value due to the underestimated interaction between electrons arrived at by the GGA-PBE method.[29] Obviously, the CB is mainly constructed by the d orbital of Ca and Zr, yet the p orbital of O and Zr form the VB. Notably, there is a similar p orbital for Zr and O, suggesting that their p orbital is coupled. Therefore, the electron of the Zr d orbital transferred to the O p orbital, and a Zr–O bond was formed.

When the host is excited by n-UV light, it is possible for electrons to jump from the O p orbital (VB) to the Zr d orbital
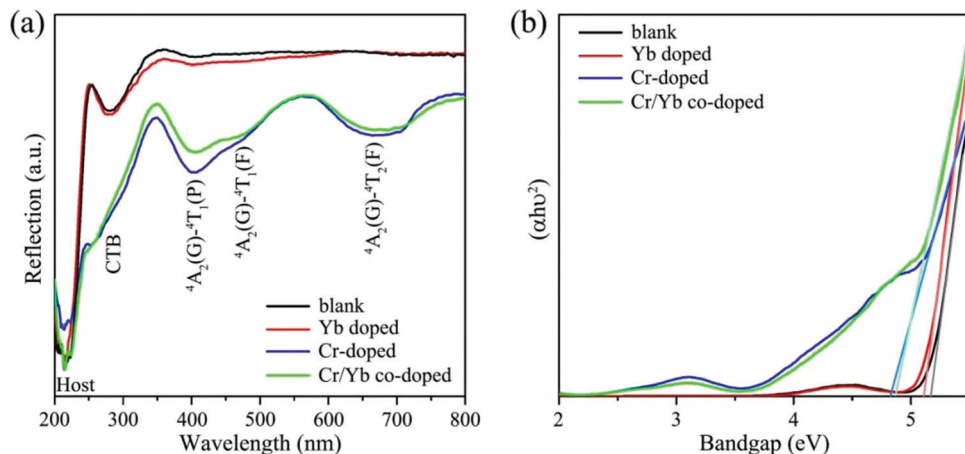
442 | *Mater. Chem. Front.*, 2022, **6**, 440–449

This journal is © The Royal Society of Chemistry and the Chinese Chemical Society 2022

Fig. 2 The (a) DRS and (b) Tucker curves of the blank, and CZGO singly or co-doped with Cr^{3+}/Yb^{3+}.
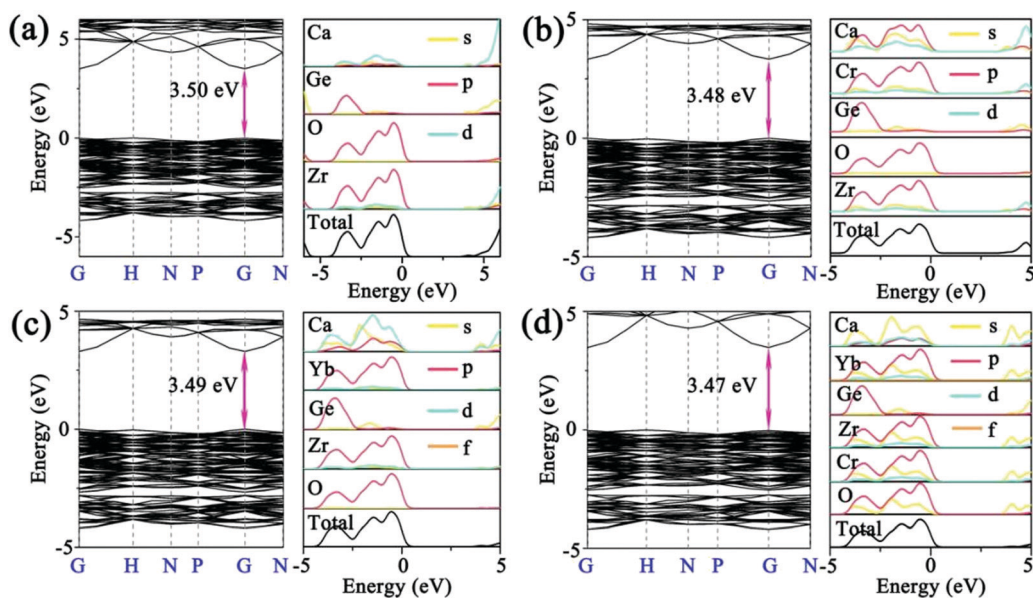

Fig. 3 The band structure and PDOS of (a) the blank, and (b) Cr-doped, (c) Yb-doped, and (d) Cr/Yb co-doped CZGO.

(CB), relax to the natural defect energy level between band gaps, and then finally travel back to the VB and emit host luminescence. Thus, a CTB might be generated between Zr and O atoms, and the host is expected to emit matrix luminescence. Additionally, the partial p and d orbitals of Ca are similar to that of Zr, resulting from Ca_2 and Zr equally sharing the 16a Wyckoff site, in which Zr and Ca possess the same symmetry and energy level splitting. After the host was doped with 1% Cr, the band gap slightly decreased to 3.48 eV (Fig. 3b). Apparently, the PDOS of Cr is similar to that of Zr, resulting from their same crystal field environment. The p orbital of Cr and O were also coupled, which might generate Cr–O CTB. Similarly, Yb was also orbitally coupled with O, indicating that the excitation of Yb^{3+} in CZGO most likely simultaneously originated from the Yb–O CTB and the energy transfer from the host or Zr–O (Fig. 3c). When the CZGO host was co-doped with 1% Cr^{3+}

and 1% Yb^{3+}, a similar PDOS was obtained for Cr, Yb, Ca, and Zr because of their site sharing (Fig. 3d). Additionally, there is a similar orbital couple of Cr and O that is expected to transfer energy to Yb^{3+} in the same manner as that to the Zr–O CTB. Additionally, the band gap reached the lowest value of 3.47 eV because a greater number of defects might be introduced in the co-doped host as compared to the singly doped host.

3.2 Luminescence properties

The PL and PLE spectra for CZGO: 1% Cr^{3+} are displayed in Fig. 4a. Under the excitation of 480 nm light, Cr^{3+} emits a broad NIR band (650–1250 nm) centered at 840 nm with a 160 nm large FWHM, corresponding to a $^4T_2(F)$–$^4A_2(F)$ transition. The PLE spectrum monitored at 840 nm consists of four bands at 280, 300, 477, and 680 nm, originating from the CTB, and $^4A_2(F)$–$^4T_1(P)$, $^4A_2(F)$–$^4T_1(F)$, and $^4A_2(F)$–$^4T_2(F)$ transitions,

Table 2 The normalized emission intensity and internal quantum yield of CZGO: $x\%Cr^{3+}$

x (%)	0.6	0.8	1.0	1.2	1.5	2.0
Normalized intensity	0.4	0.7	1.0	0.8	0.7	0.5
QY (%)	14	23	35	26	22	18

respectively. To optimize the luminescence intensity, various concentrations of CZGO: $x\%$ Cr^{3+} (x = 0.6, 0.8, 1.0, 1.2, 1.5, and 2.0) were synthesized, and their normalized integrated emission intensities and quantum yield (QY) are listed in Table 2. The emission intensity continuously increases until the concentration of Cr^{3+} becomes greater than 1.0%, which occurs due to the concentration quenching effect. The QY reaches the maximum value of 35% when the amount of Cr^{3+} equals 1%.

The emission of Cr^{3+} is strongly dependent on the crystal field environment of the octahedron (O_h symmetry), in which the crystal field strength and splitting can be roughly estimated by the Tanabe–Sugano theory using the following equations:[30]

$$10Dq = E(^4A_2 - {}^4T_2) \quad (5)$$

where D_q denotes the crystal field strength, and the Rach parameter B can be calculated by:

$$\frac{D_q}{B} = \frac{15(x-8)}{x^2 - 10x} \quad (6)$$
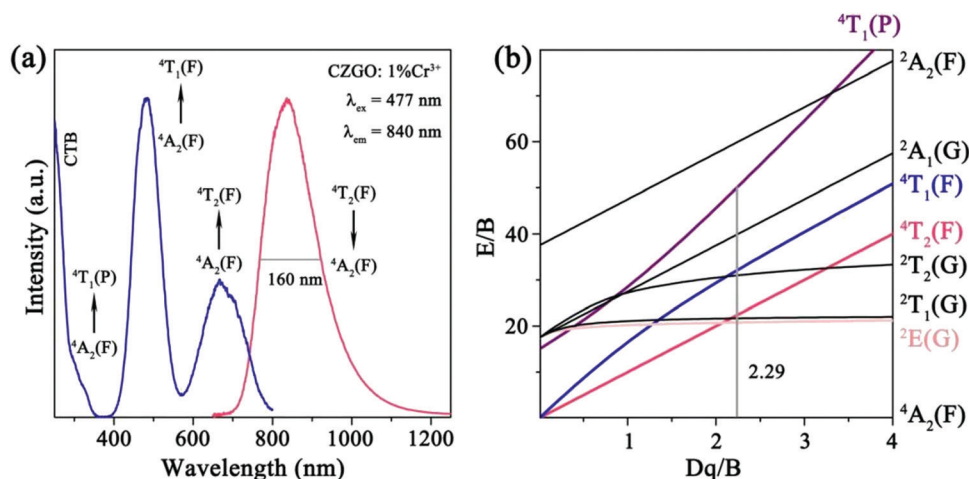
in which x is defined as:

$$x = \frac{E(^4A_2 - {}^4T_1) - E(^4A_2 - {}^4T_2)}{D_q} \quad (7)$$

$E(^4T_1 - {}^4A_2)$ and $E(^4T_2 - {}^4A_2)$ were determined to be 20 964 and 14 706 cm^{-1}, respectively. Accordingly, D_q, B, and D_q/B were calculated to be 1470 cm^{-1}, 642 cm^{-1}, and 2.29, respectively (Fig. 4b). The D_q/B value was slightly less than 2.3, which indicates that the crystal field strength for Cr^{3+} in CZGO is weak, and $^4T_2(F)$ is below the $^2E(G)$ level.[31] Consequently, Cr^{3+} emits a broad NIR emission band, derived from the $^4T_2(F) - {}^4A_2(F)$ transition.

As predicted above by the first-principles theory calculation in Fig. 3a, host emission is expected, and a band emission centered at 740 nm was displayed (Fig. 5a). Additionally, the PLE spectrum includes a strong excitation band centered at 280 nm, which was assigned to the electron transition from the O-p to Zr-d orbital in the Zr–O CTB. The corresponding experimental band gap is approximately 5.1 eV, which is greater than that obtained by theoretical calculation (E_g = 3.5 eV) due to the underestimates of the atomic reaction. However, the emission peak (740 nm, 1.68 eV) is far less than the value of the band gap, and this can be inferred as a defect energy level that is caused by an oxygen vacancy.

To confirm our speculation and reveal the mechanism of matrix luminescence, the band structure and DOS of the matrix with one oxygen vacancy were calculated. As shown in Fig. 5b and c, a defect energy level can be easily observed after introducing an oxygen vacancy (V_o), and the energy difference between the defect and the VB was calculated to be 1.8 eV (approximately 689 nm), which is very close to the emission peak (740 nm). Accordingly, the coupling of the orbitals constructs the Zr–O CTB, which corresponds to the excitation band. The defect energy level most likely originates from the oxygen vacancy, and the transition between the defect and VB forms the emission band. Consequently, the detailed mechanism of the matrix luminescence consists of an electron that is pumped from the VB (O-p orbital) to the CB (Zr-d orbital) by n-UV light (280 nm), transfers to the defect energy level (V_o) by non-radiation relaxation (NR), and then immediately returns to the VB and subsequently releases far-red light (Fig. 5d).

To further refine the practical application value, Yb^{3+} was introduced into CZGO: Cr^{3+} to broaden the FWHM by energy transfer from the Cr^{3+} to Yb^{3+} ion. For a comprehensive understanding of the energy transfer between the host or Cr^{3+} and Yb^{3+}, the PL and PLE spectra of the blank, and Yb^{3+}-doped and Cr^{3+}–Yb^{3+} co-doped samples are displayed in Fig. 6a. The Yb^{3+} singly doped CZGO exhibits two emission bands at 750 nm – one from the host, and one typical emission band centered at 968 nm from the $^2F_{7/2} \rightarrow {}^2F_{5/2}$ transition of Yb^{3+}. A comparison

Fig. 4 (a) The PL and PLE spectra together with (b) a Tanabe–Sugano energy level diagram of Cr^{3+} in CZGO.

This journal is © The Royal Society of Chemistry and the Chinese Chemical Society 2022
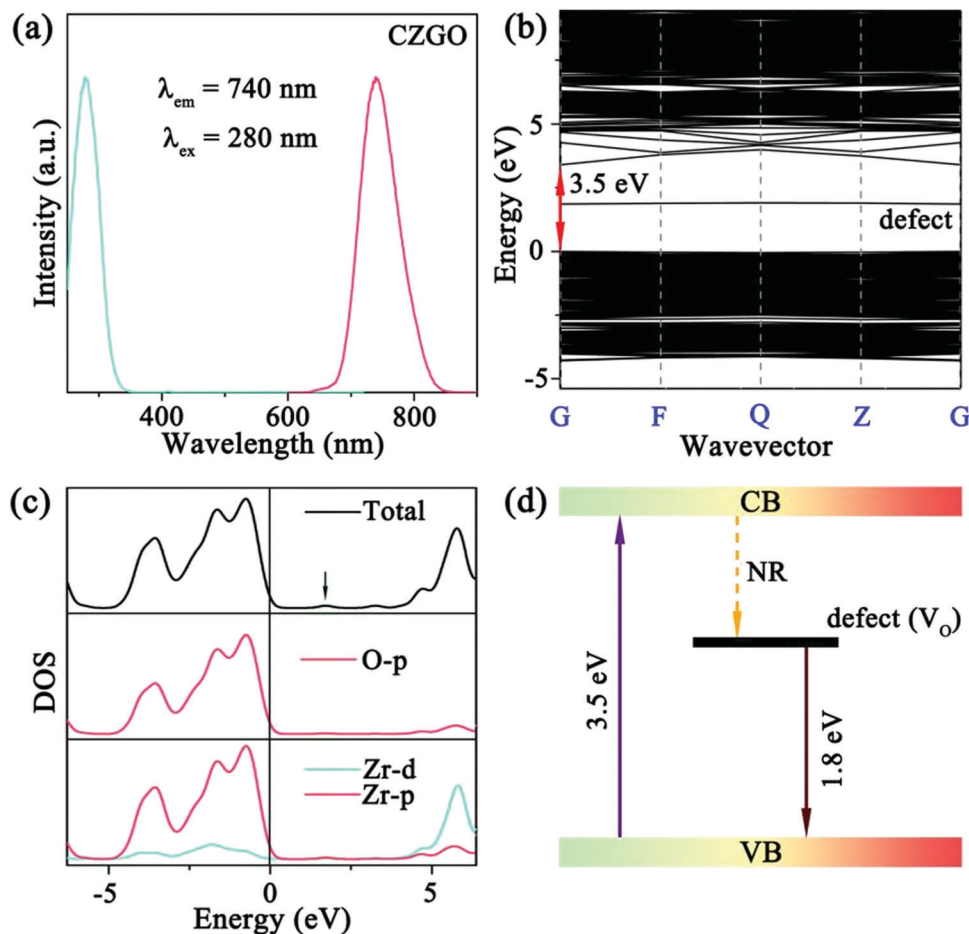
Fig. 5 (a) The PL and PLE spectra of the blank; (b) the band structure and (c) DOS of CZGO with an oxygen vacancy (V_O) together with (d) the mechanism of the matrix luminescence.

of the PL and PLE spectra of the host and CZGO: 1% Yb^{3+} confirms that the excitation bands of singly doped Yb^{3+} are the same as those of the host, which implies that energy was transferred from the Zr–O CTB to Yb^{3+}.

Although there is no overlap between the excitation band of Yb^{3+} and the emission band of Cr^{3+}, there is also a significant energy transfer process from Cr^{3+} to Yb^{3+} because the PLE spectra of Yb^{3+} is the same as that of Cr^{3+}, except for the intensity in Cr^{3+}–Yb^{3+} co-doped CZGO. As mentioned above, similar to Zr, Cr^{3+} enters into the ZrO_6 site and couples with O in the p orbital, so that Cr^{3+} can also realize energy transfer to Yb^{3+} in the same manner as that which occurred with Zr–O CTB. To obtain the most optimal luminescence properties, the emission spectra of CZGO: 1% Cr^{3+}, y% Yb^{3+} (y = 0, 1, 2, 3, 4) were measured and are provided in Fig. 6b as a function of the concentration of Yb^{3+}. With increasing Yb^{3+}, the FWHM increased from 160 to 230 nm after doping 1% Yb^{3+} into CZGO: 1% Cr^{3+}, and the integrated emission intensity was maintained at 73% of CZGO singly doped with Cr^{3+}.

To further verify the energy transfer process between Cr^{3+} and Yb^{3+}, decay curves of Cr^{3+} in CZGO: 1% Cr^{3+}, y% Yb^{3+} (y = 0, 1, 2, 3, 4) were measured and are depicted in Fig. 6c. These can

be well fitted by second-order exponential functions according to the following equation:[32]

$$I_t = A_1 \exp\left(-\frac{t}{\tau_1}\right) + A_2 \exp\left(-\frac{t}{\tau_2}\right) \quad (8)$$

where I_t represents the luminescence intensity at time t, A_1 and A_2 denote constants, and τ_1 and τ_2 denote the decay times for exponential components. The average lifetime can be estimated by:

$$\tau_s = \frac{A_1\tau_1^2 + A_2\tau_2^2}{A_1\tau_1 + A_2\tau_2} \quad (9)$$

As the concentration of Yb^{3+} increased from 0 to 4%, the calculated average lifetime of Cr^{3+} monitored at 840 nm gradually decreased from 68.5 to 42.9 μs, verifying the existence of an efficient energy transfer between Cr^{3+} and Yb^{3+}. As shown in Fig. 6d, under near-ultraviolet or blue/red light irradiation, the electrons of Cr^{3+} jump from ground state $^4A_2(G)$ to excited states, and then relax to the lowest excited state $^4T_2(F)$. Next, some of them return to the ground state $^4A_2(G)$ and emit a broad NIR band centered at 840 nm, while others transfer their energy to Yb^{3+} ions, and the electrons at $^2F_{5/2}$ are excited to $^2F_{7/2}$. Finally, the electrons return to $^2F_{5/2}$ and also release a
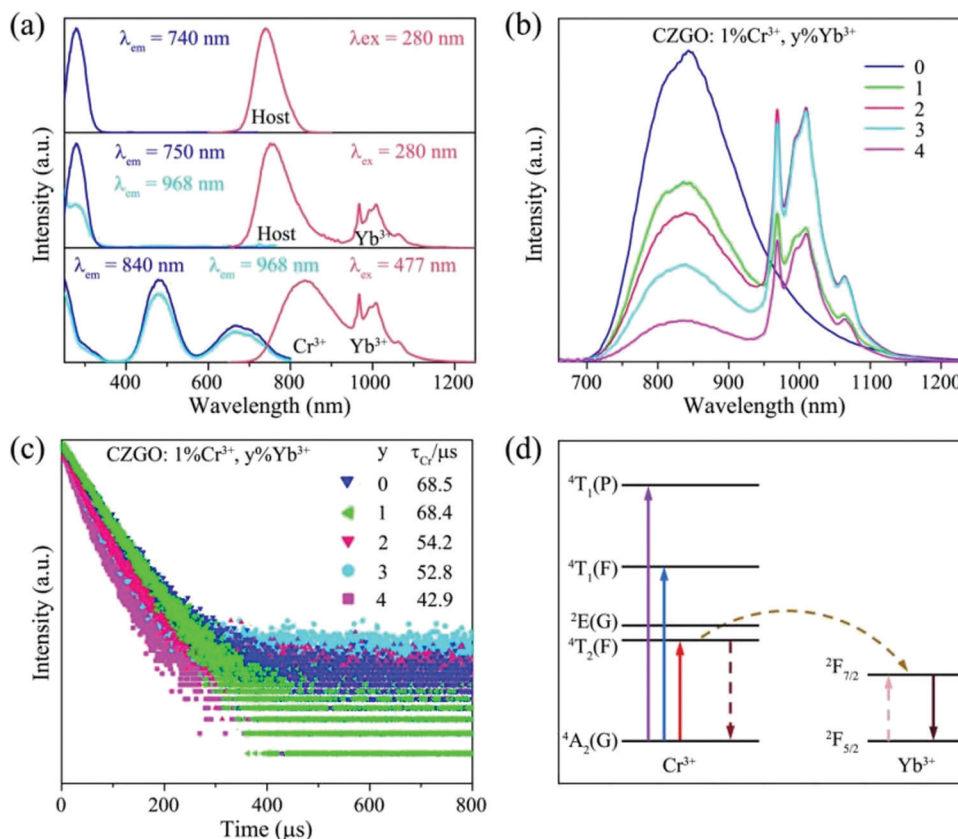
Fig. 6 (a) The PL and PLE spectra of the blank, and Yb^{3+}-doped and Cr^{3+}/Yb^{3+}-co-doped CZGO; (b) PL spectra and (c) decay curves of CZGO: 1% Cr^{3+}, y% Yb^{3+} (y = 0, 1, 2, 3, 4) excited by 480 nm light together with (d) an energy transfer schematic diagram between Cr^{3+} and Yb^{3+}.

wide emission band with peaks at 968 and 1009 nm. Consequently, the FWHM of CZGO: Cr^{3+} is considerably broadened from 160 to 230 nm by the introduction of Yb^{3+}.

3.3 Thermal stability

The thermal stability of phosphors coated on LED chips plays an important role in the process of deriving practical applications, because the operating temperature of LEDs is always greater than 100 °C (373 K). To evaluate the thermal stability, the temperature-dependent emission spectra of singly doped Cr^{3+} and Cr^{3+}/Yb^{3+} co-doped CZGO were obtained and are displayed in Fig. 7a and b, respectively. With increasing temperature, the emission intensity of Cr^{3+}-doped CZGO gradually decreased, but the emission position did not change. After CZGO: Cr^{3+} was doped with Yb^{3+}, the Cr^{3+} in the co-doped sample exhibited the same thermal quenching behavior as the singly doped sample, but higher thermal resistance was exhibited by Yb^{3+}. As shown in Fig. 7c, at the operating temperature of LEDs (373 K), the emission intensity of CZGO: Cr^{3+} and CZGO: Cr^{3+}/Yb^{3+} was maintained 69% and 73% of the initial intensity at room temperature, respectively. Obviously, the thermal stability was increased with the introduction of Yb^{3+}, which also occurred with Ca$_2$LuZr$_2$Al$_3$O$_{12}$.[15] The thermal quenching mechanism is illustrated in the configuration coordinate diagram shown in Fig. 7d. Electrons at ground state ^{4}A$_2$(F) are pumped to excited states and then relax to the lowest excited state ^{4}T$_2$(F), where a portion of them absorb additional thermal vibration energy to reach the cross point between

^{4}A$_2$(F) and ^{4}T$_2$(F). When the electrons return to the ground state by cross-relaxation, thermal quenching ensues. The additional energy is defined as thermal activation energy ΔE_a, which can be estimated by the following equation:[33]

$$I(T) = \frac{I_0}{1 + c\exp(\Delta E_a / k_B T)} \qquad (10)$$

where I_0 and $I(T)$ represent the integrated emission intensity at the initial temperature and temperature T, c denotes a constant, and k_B denotes the Boltzmann constant (k_B = 8.62 × 10^{-5} eV). The calculated ΔE_a of CZGO: Cr^{3+}/Yb^{3+} is 4.3 eV, which is higher than that of CZGO: Cr^{3+} (3.8 eV). However, the Cr^{3+} emission exhibits the same thermal quenching behavior in the CZGO: Cr^{3+} and CZGO: Cr^{3+}/Yb^{3+} systems, suggesting that the enhancement of thermal resistance is due to the introduction of Yb^{3+} instead of the improvement in ΔE_a. This occurs because Yb^{3+} possesses the simple ground state ^{2}F$_{5/2}$ and excited state ^{2}F$_{7/2}$, which effectively prevents energy loss due to cross-relaxation between different energy levels. On the contrary, the thermal quenching behavior of Yb^{3+} is mainly dominated by multi-phonon emission, and the thermal quenching intensity is always less than that of the cross-relaxation effect.[14] Therefore, the increased thermal stability is described as the transfer of energy from Cr^{3+} to the more stable Yb^{3+}. It can also be predicted that the thermal stability of the sample will be further increased with increasing Yb^{3+}, but the emission intensity and FWHM will decrease.

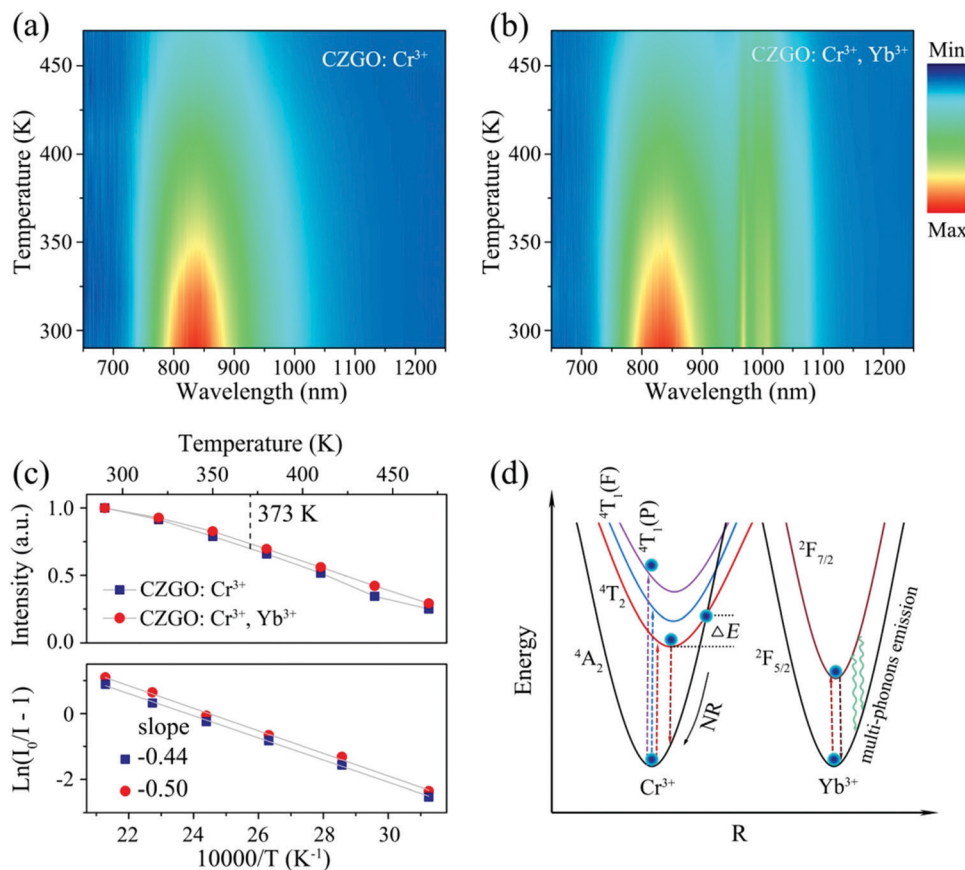**446** | *Mater. Chem. Front.*, 2022, **6**, 440–449

This journal is © The Royal Society of Chemistry and the Chinese Chemical Society 2022

Fig. 7 The temperature-dependent PL spectra of (a) 1% Cr^{3+} and (b) 1% Cr^{3+}/1% Yb^{3+} co-doped CZGO; (c) normalized integrated intensity and a plot of $\ln(I_0/I - 1)$ vs. 10 000/T for Cr^{3+} and Cr^{3+}/Yb^{3+} co-doped CZGO; (d) a configuration coordinate diagram for Cr^{3+} and Yb^{3+} in the CZGO host.

3.4 Packaged NIR pc-LED application characteristics

NIR light sources have been widely applied for night vision and bio-imaging because they are invisible to human eyes and possess satisfactory bio-penetration.[34] Aimed at these applications, we fabricated a NIR pc-LED by combining a 450 nm commercial chip with CZGO: Cr^{3+}/Yb^{3+}, which consists of a blue and broadband NIR spectra (Fig. 8a). Fig. 8b shows photographs of fruits and a hand illuminated by the white LED and fabricated NIR pc-LED light sources. The fruits are colorful under the white LED illumination, while a black and
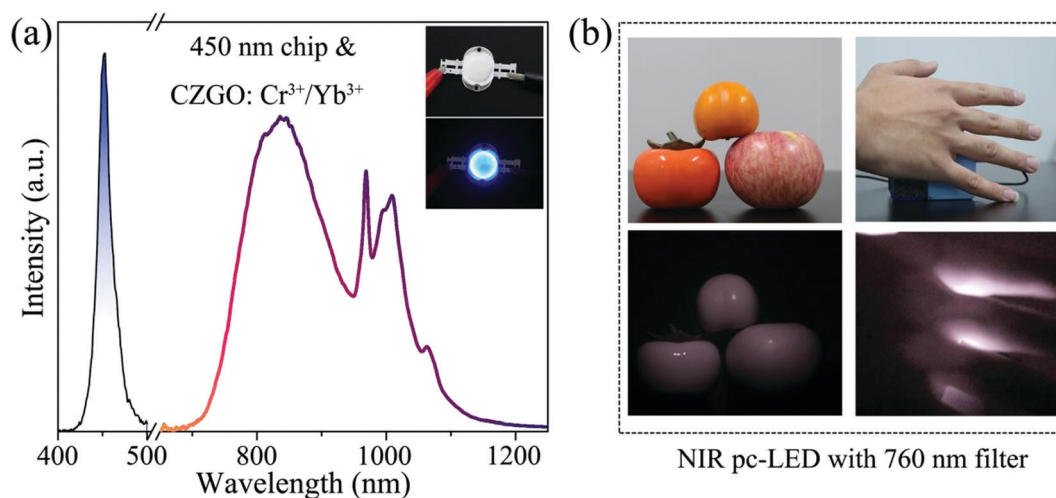

Fig. 8 (a) The output spectrum of fabricated NIR pc-LED packaged by combining a 450 nm chip with CZGO: Cr^{3+}/Yb^{3+}. The inset shows the fabricated LED devices. (b) Photographs of various fruit and a hand under a white LED and NIR pc-LED with a 760 nm filter.

white image appears when they are illuminated by the fabricated NIR pc-LED. Additionally, the hand is covering the fabricated NIR pc-LED light source, and some blood vessels in the hand can be clearly observed by a Canon camera with a 760 nm filter, which confirms that the bio-penetration of the NIR light source is satisfactory. These features indicate that CZGO: Cr^{3+}/Yb^{3+} possesses considerable potential for use in night vision and bio-imaging.

4. Conclusions

Using a high-temperature solid-state reaction method, we developed a NIR phosphor CZGO: Cr^{3+} that exhibits a broad emission band ranging from 650 to 1250 nm with a FWHM of 160 nm. Based on first-principles theory calculation, it was determined that the formation of CTBs occurred due to the p orbital coupling of Zr^{4+}, Cr^{3+}, Yb^{3+}, and O^{2-} atoms, and the host luminescence most likely originated from the electron transition between the d orbital of Zr^{4+} and the p orbital of O^{2-}.

By comparing the formation energy, the site-selective occupancy was revealed as the Cr^{3+} and Yb^{3+} preferring to enter into the ZrO_6 and CaO_8 polyhedrons, respectively. Utilizing the introduction of Yb^{3+}, the FWHM of Cr^{3+} was further broadened to 230 nm, and the thermal stability was also increased by effective energy transfer from Cr^{3+} to the more stable Yb^{3+} ions. The energy transfer process was also investigated by spectroscopy and decay curves. Finally, a NIR pc-LED was fabricated by combining CZGO: Cr^{3+}, Yb^{3+} with a 460 nm LED chip, which exhibited a satisfactory bio-penetration ability and night vision features. These results illustrate that there is potential application for CZGO: Cr^{3+}, Yb^{3+} in non-destructive detection and night vision.

Author contributions

Jinmeng Xiang was responsible for performing the experiments, analyzing the data, and writing the first draft. The contributor's roles were conceptualization, investigation, and writing the original draft. Jiming Zheng was responsible for assisting with theoretical calculations. Xiaoqi Zhao was responsible for testing the low-temperature spectrum and packaging the LED device. The contributor's role was providing partial resources. Xue Zhou was responsible for assisting with partial experiments. The contributor's role was data curation. Changheng Chen was responsible for analyzing the thermal quenching mechanism. The contributor's role was validation. Minkun Jin was responsible for assisting with partial graphics. The contributor's role was software. Chongfeng Guo was responsible for the supervision and leadership of the overall work. The contributor's roles were conceptualization, funding acquisition, project administration, supervision, and writing-review and editing.

Conflicts of interest

There are no conflicts to declare.

Acknowledgements

References

1 E. H. Song, H. Ming, Y. Y. Zhou, F. Q. He, J. C. Wu, Z. G. Xia and Q. Y. Zhang, Cr^{3+}-doped Sc-based fluoride enabling highly efficient near infrared luminescence: a case study of K_2NaScF_6: Cr^{3+}, *Laser Photonics Rev.*, 2021, **15**, 2000410.

2 Y. Wei, Z. Y. Gao, X. H. Yun, H. Yang, Y. X. Liu and G. G. Li, Abnormal Bi^{3+}-activated NIR emission in highly symmetric $XAl_{12}O_{19}$ (X = Ba, Sr, Ca) by selective sites occupation, *Chem. Mater.*, 2020, **32**, 8747–8753.

3 Z. Y. Yang, Y. F. Zhao, Y. Y. Zhou, J. W. Qiao, Y. C. Chuang, M. S. Molokeev and Z. G. Xia, Giant red-shifted emission in $(Sr,Ba)Y_2O_4$: Eu^{2+} phosphor toward broadband near-infrared luminescence, *Adv. Funct. Mater.*, 2021, 2103928–2103939.

4 B. B. Su, M. Z. Li, E. H. Song and Z. G. Xia, Sb^{3+}-doping in cesium zinc halide single crystals enabling high-efficiency near-infrared emission, *Adv. Funct. Mater.*, 2021, **31**, 2105316.

5 J. W. Qiao, G. J. Zhou, Y. Y. Zhou, Q. Y. Zhang and Z. G. Xia, Divalent europium-doped near-infrared-emitting phosphor for light-emitting diodes, *Nat. Commun.*, 2019, **10**, 5267–5273.

6 Z. W. Jia, C. X. Yuan, Y. F. Liu, X. J. Wang, P. Sun, L. Wang, H. C. Jiang and J. Jiang, Strategies to approach high performance in Cr^{3+}-doped phosphors for high-power NIR-LED light sources, *Light: Sci. Appl.*, 2020, **9**, 86–94.

7 X. F. Zhou, W. Y. Geng, J. Y. Li, Y. C. Wang, J. Y. Ding and Y. H. Wang, An ultraviolet-visible and near-infrared-responded broadband NIR phosphor and its NIR spectroscopy application, *Adv. Opt. Mater.*, 2020, 1902003.

8 C. P. Wang, X. M. Wang, Y. Zhou Yang, S. Zhang, C. Li, D. F. Hu, L. Xu and H. Jiao, An ultra-broadband near-infrared Cr^{3+}-activated gallogermanate $Mg_3Ga_2GeO_8$ phosphor as light sources for food analysis, *ACS Appl. Electron. Mater.*, 2019, **1**, 1046–1053.

9 V. Rajendran, M. Fang, N. D. G. Guzman, T. Lesniewski, S. Mahlik, M. Grinberg, G. Leniec, M. S. Kaczmarek, Y. Lin, K. Lu, C. Lin, H. Chang, S. Hu and R. S. Liu, Super broadband near-infrared phosphors with high radiant flux as future light sources for spectroscopy applications, *ACS Energy Lett.*, 2018, **3**, 2679–2684.

10 L. L. Zhang, D. D. Wang, Z. D. Hao, X. Zhang, G. H. Pan, H. J. Wu and J. H. Zhang, Cr^{3+}-doped broadband NIR garnet phosphor with enhanced luminescence and its application in NIR spectroscopy, *Adv. Opt. Mater.*, 2019, 1900185.

11 D. C. Yu, Y. S. Zhou, C. S. Ma, J. M. Melman, K. M. Baroudi, M. LaCapra and R. E. Riman, Non-rare-earth Na_3AlF_6: Cr^{3+} phosphors for far-red light-emitting diodes, *ACS Appl. Electron. Mater.*, 2019, **1**, 2325–2333.

12 Q. Wei, J. Y. Ding and Y. H. Wang, A novel tunable extra-broad yellow-emitting nitride phosphor with zero-thermal-quenching property, *Chem. Eng. J.*, 2020, **386**, 124004.

13 B. Bai, P. P. Dang, D. Y. Huang, H. Z. Lian and J. Lin, Broadband near-infrared emitting $Ca_2LuScGa_2Ge_2O_{12}$: Cr^{3+} phosphors: luminescence properties and application in light-emitting diodes, *Inorg. Chem.*, 2020, **59**, 13481–13488.

14 X. X. Xu, Q. Y. Shao, L. Q. Yao, Y. Dong and J. Q. Jiang, Highly efficient and thermally stable Cr^{3+}-activated silicate phosphors for broadband near-infrared LED applications, *Chem. Eng. J.*, 2020, **383**, 123108.

15 H. T. Zeng, T. L. Zhou, L. Wang and R. J. Xie, Two-site occupation for exploring ultra-broadband near-infrared phosphor-double-perovskite La_2MgZrO_6: Cr^{3+}, *Chem. Mater.*, 2019, **31**, 5245–5253.

16 G. C. Liu, T. Hu, S. Maxim Molokeev and Z. G. Xia, Li/Na substitution and Yb^{3+} co-doping enabling tunable near-infrared emission in $LiIn_2SbO_6$: Cr^{3+} phosphors for lighting-emitting diodes, *iScience*, 2021, **24**, 102250.

17 L. Q. Yao, Q. Y. Shao, S. Y. Han, C. Liang, J. H. He and J. Q. Jiang, Enhancing near-infrared photoluminescence intensity and spectral properties in Yb^{3+} co-doped $LiScP_2O_7$: Cr^{3+}, *Chem. Mater.*, 2020, **32**, 2430–2439.

18 L. Q. Yao, Q. Y. Shao, X. X. Xue, Y. Dong, C. Liang, J. H. He and J. Q. Jiang, Broadband emission of single-phase $Ca_3Sc_2Si_3O_{12}$: Cr^{3+}/Ln^{3+} (Ln = Nb, Yb, Ce) phosphors for novel solid-state light sources with visible to near-infrared light output, *Ceram. Int.*, 2019, **45**, 14249–14255.

19 Q. Y. Shao, H. Ding, L. Q. Yao, J. F. Xu, C. Liang, Z. H. Li, Y. Dong and J. Q. Jiang, Broadband near-infrared light source derived from Cr^{3+}-doped phosphors and a blue LED chip, *Opt. Lett.*, 2018, **43**, 5251–5254.

20 S. He, L. L. Zhang, H. Wu, H. J. Wu, G. H. Pan, Z. D. Hao, X. Zhang, L. G. Zhang, H. Zhang and J. H. Zhang, Efficient super broadband NIR $Ca_2LuZr_2Al_3O_{12}$: Cr^{3+}, Yb^{3+} garnet phosphor for pc-LED light source toward NIR spectroscopy applications, *Adv. Opt. Mater.*, 2020, 1901684.

21 W. D. Nie, Y. Li, J. X. Zuo, Y. K. Kong, W. F. Zou, G. Chen, J. Q. Peng, F. Du, L. Han and X. Y. Ye, Cr^{3+}-activated $Na_3X_2Li_3F_{12}$ (X = Al, Ga, In) garnet phosphors with broad-band NIR emission and high luminescence efficiency for potential biomedical application, *J. Mater. Chem. C*, 2021, **9**, 15230–15241.

22 E. T. Basore, W. G. Xiao, X. F. Liu, J. H. Wu and J. R. Qiu, Broadband near-infrared garnet phosphors with near-unity internal quantum efficiency, *Adv. Opt. Mater.*, 2020, 2000296.

23 B. H. Toby, EXPGUI, a graphical user interface for GASA, *J. Appl. Crystallogr.*, 2001, **34**, 210–213.

24 M. D. Segall, P. J. D. Lindan, M. J. Probert, C. J. Pickard, P. J. Hasnip, S. J. Clark and M. C. Payne, First-principles simulation: ideas, illustrations and the CASTEP code, *J. Phys.: Condens. Matter*, 2002, **14**, 2717–2744.

25 M. Ernzerhof and G. E. Scuseria, Assessment of the Perdew-Burke-Ernzerhof exchange-correlation functional, *J. Chem. Phys.*, 1999, **110**, 5029–5036.

26 R. D. Shannon, Revised effective ionic radii and systematic studies of interatomic distance in halides and chalcogenides, *Acta Crystallogr., Sect. A: Cryst. Phys., Diffr., Theor. Gen. Crystallogr.*, 1976, **32**, 751–767.

27 J. W. Lee, S. P. Singh, M. Kim, S. U. Hong, W. B. Park and K. S. Sohn, Metaheuristics-assisted combinatorial screening of Eu^{2+}-doped Ca-Sr-Ba-Li-Mg-Al-Si-Ge-N compositional space in search of a narrow-band green emitting phosphor and density functional theory calculations, *Inorg. Chem.*, 2017, **56**, 9814–9824.

28 A. A. Christy, O. M. Kvalheim and R. A. Velapoldi, Quantitative analysis in diffuse reflectance spectrometry: A modified Kubelka-Munk equation, *Vib. Spectrosc.*, 1995, **9**, 19–27.

29 J. Zhu, M. H. Yang, Y. Che, Z. H. Zhang, X. C. Ge, J. Y. Xiang, Y. Zhou, K. Xiong and H. W. Yu, Structure-optical behavior correlation, optimized photoluminescence, and DFT calculation of $La_7O_6(BO_3)(PO_4)_2$: Sm^{3+} micropowder for solid state lighting, *ACS Appl. Electron. Mater.*, 2019, **1**, 1688–1697.

30 Z. W. Zhou, J. M. Zheng, R. Shi, N. M. Zhang, J. Y. Chen, R. Y. Zhang, H. Suo, G. M. Ewa and C. F. Guo, *Ab initio* site Occupancy and far-red emission of Mn^{4+} in cubic-phase $La(MgTi)_{1/2}O_3$ for plant cultivation, *ACS Appl. Mater. Interfaces*, 2017, **9**, 6177–6185.

31 H. H. Lin, G. X. Bai, T. Yu, M. K. Tsang, Q. Y. Zhang and J. H. Hao, Site occupancy and near-infrared luminescence in $Ca_3Ga_2Ge_3O_{12}$: Cr^{3+} persistent phosphor, *Adv. Opt. Mater.*, 2017, **5**, 1700227.

32 J. M. Xiang, J. M. Zheng, Z. W. Zhou, H. Suo, X. Q. Zhao, X. J. Zhou, N. M. Zhang, M. S. Molokeev and C. F. Guo, Enhancement of red emission and site analysis in Eu^{2+} doped new-type structure $Ba_3CaK(PO_4)_3$ for plant growth white LEDs, *Chem. Eng. J.*, 2019, **356**, 236–244.

33 H. J. Yu, J. Chen, R. Y. Mi, J. Y. Yang and Y. G. Liu, Broadband near-infrared emission of K_3ScF_6: Cr^{3+} phosphors for night vision imaging system sources, *Chem. Eng. J.*, 2021, **417**, 129271.

34 X. Zhou, J. M. Xiang, J. M. Zheng, X. Q. Zhao, H. Suo and C. F. Guo, *Ab initio* two-sites occupancy and broadband near-infrared emission of Cr^{3+} in Li_2MgZrO_4, *Mater. Chem. Front.*, 2021, **5**, 4334–4342.